Chapter 3

Hydrogen Evolution and Oxygen Evolution Reactions of Pristine and Alkali Metal Doped $SnSe_2$ Monolayer

3.1 Introduction

The challenge of global warming, primarily driven by the extensive use of fossil fuels [1], could potentially be addressed by adopting eco-friendly methods to harness green and clean energy. One particularly clean approach to energy production involves utilizing hydrogen (H_2) as a fuel, which can be generated by splitting of water molecules into its elemental components through a process known as water-splitting. H_2 finds application not only in energy generation but also in industries like chemicals, for producing ammonia and methanol. Moreover, its potential uses extend to powering vehicles, fuel cells, heating systems, aircraft, and even sulfur removal from petroleum [2-4]. Among the various available techniques for H_2 production, the electrochemical splitting of water, employing photocatalysts, electrocatalysts, or photoelectrocatalysts, has garnered significant attention due to its capacity for producing H_2 without any harmful emissions [5-10]. This water-splitting process involves two half reactions: the evolution of H_2 through $2H^+ + 2e^- \rightarrow H_2$ reaction, and the evolution of O_2 through $2H_2O \rightarrow 4H^+ + 4e^- + O_2$. The distinction between photocatalytic and electrocatalytic approaches for the hydrogen evolution reaction (HER) lies in how the charge carriers are generated. Photocatalysis relies on absorbing sunlight to generate carriers, whereas electrocatalysis involves direct electron transfer through lower-potential chemical reactions. Materials aiming to serve as electrocatalysts, photocatalysts, or electro-photocatalysts must fulfill specific criteria. An effective electrocatalyst should have lower overpotential required for the chemical reaction. On the other hand, a suitable photocatalyst requires a moderate electronic band gap (approximately 1-2 eV) to facilitate absorption of optical photons. To qualify as a photocatalyst or an electro-photocatalyst, materials must meet these necessary conditions,

$$E \geq E_g + E_a \text{ and } E \geq E_g + E_{AOP} \tag{3.1}$$

In the context of this discussion, several key parameters come into play. E represents the minimum energy required to initiate the water molecule splitting process, while E_g stands for the bandgap of catalyst. E_a denotes the activation energy specific to a photocatalyst, and E_{AOP} signifies the activation overpotential [6]. To date, there has been substantial progress in the development of promising catalysts for HER. These catalysts utilize non-noble transition metals, carbides, transition metal phosphides, cobalt phosphide in pyrite form, and graphene, arsenene, and other materials doped with elements like nitrogen or boron [5-7,11-16]. Despite these advancements, the overall efficiency of H_2 production, a parameter influenced by the overpotential of the electrocatalyst, still lacks a viable alternative to the traditionally employed, costly noble metals [5,17].

A notable observation is that the edges of metal chalcogenides exhibit higher reactivity compared to their basal planes, posing a challenge for H_2 production [18]. To address this limitation, an effective strategy involves increasing the proportion of edges to basal planes in these materials. Among metal chalcogenides, $SnSe_2$ falls under the same category as MoS_2 and WS_2, which have gained attention as potential electrocatalysts due to their cost-effective fabrication and improved electrocatalytic performance [5]. Utilizing DFT, a study by Han et al. [19] revealed that a monolayer of $SnSe_2$ displays semiconducting behaviour with a band gap of 0.85 eV. This suggests the potential application of $SnSe_2$ as an electrocatalyst for HER activity. Notably, introducing doping into $SnSe_2$ induces a metallic character that enhances HER activity on its basal plane [5,15]. This effect is reflected in the density of states (DOS) plots at the Fermi level for various dopants i.e Na, K, and Ca. Modifying the electronic properties of materials to enhance HER and/or OER activities can be achieved through external strain, electric fields, and doping [15,20,21]. A DFT-based study demonstrates that applying tensile strain to the $SnSe_{2(1-x)}S_{2x}$ monolayer on its basal plane enhances HER catalytic activity [22]. Other reports on 2D materials such as borophene [23], graphene [24], and nanosheets [25]

suggest that doping these materials with alkali metals significantly improves their HER performance. Among these, Li-doped borophene exhibits the highest reported capacity [23]. Wang et al. embarked on a comprehensive exploration of the hydrogen storage capabilities of borophene, specifically focusing on three different polytypes of borophene synthesized on an Ag substrate. The investigation extended to the impact of alkali-metal (Li, Na, and K) doping on borophene. The findings unveiled a robust binding affinity between alkali-metal atoms and borophene. Interestingly, it was observed that the presence of metal atoms dispersed individually on the borophene surface and was energetically more favourable compared to the formation of metal clusters, which helped mitigate aggregation issues. The primary mechanism at play in hydrogen molecule (H_2) adsorption was polarization, and the achieved storage capacities were intricately tied to the configurations of the borophene, the types of foreign atoms introduced, and the ensuing electronic interactions. Furthermore, they accounted for the effects of temperature and pressure using a modified version of the van't Hoff equation. The results conclusively suggest that borophene structures doped with Na in the S2 and S3 configurations and Li in all three types of borophene hold substantial promise as prospective candidates for hydrogen storage applications [23].

In our current investigation, we have explored the structural and electronic characteristics of pristine and doped tin-diselenide ($SnSe_2$) and have described the influence of doping (Na, K, and Ca) on the HER and OER catalytic activities, work function, and optical properties of $SnSe_2$, using dispersion corrected DFT calculations. Additionally, we've delved into the interaction mechanisms between hydrogen and oxygen atoms with both pristine and doped $SnSe_2$ to enhance its electrocatalytic performance.

3.2 Computational Methods

The computations in this study utilized advanced first-principles density functional theory

(DFT) through the Quantum Espresso code [26]. The calculations involved simulating the behaviour of molecules and materials at the atomic level. To accurately describe the electron interactions, the Perdew-Burke-Ernzerhof (PBE) generalized gradient approximation (GGA) was employed for the exchange-correlation interactions [27]. Additionally, Grimme's dispersion correction (D2) was applied to improve the accuracy of adsorption energy calculations for H and O adsorption. To ensure reliable results, specific parameters were set: kinetic energy and charge density cut-offs of 80 and 800 Ry, respectively, were chosen to ensure convergence of lattice parameters and total energy within specified limits. To prevent interactions between neighbouring layers, a vacuum layer with a thickness of 15 Å was introduced above the monolayer structure. The sampling of the reciprocal space was achieved using a dense grid of dimensions 9x9x1 under the Monkhorst-Pack scheme [28]. Convergence of the calculations was ensured by monitoring the energy change between consecutive steps, with a threshold of 10^{-4} eV. The calculations iterated until the forces acting on each atom were minimized to less than 0.001 eV/Å, ensuring the atomic positions reached a stable state. Furthermore, the study involved assessing the optical absorption spectra of both pristine and doped-$SnSe_2$ materials to evaluate their potential for use as photo-electrocatalysts. The optical absorption spectra were determined using the frequency-dependent dielectric function, which describes how a material interacts with light. The real and imaginary components of the dielectric function, represented as $\varepsilon(\omega)=\varepsilon_{real}(\omega)+\varepsilon_{imag}(\omega)$, were obtained using the Kramers-Kronig relation. This approach helped to gain insights into the materials ability to absorb light and potentially drive electrocatalytic processes. The Kramers-Kronig related is,

$$\boldsymbol{\alpha = \frac{2\sqrt{2}\pi e}{hc}\sqrt{\sqrt{\varepsilon_{real}^2(\omega) + \varepsilon_{imag}^2(\omega)} - \varepsilon_{real}(\omega)}} \tag{3.2}$$

Here, in equation (3.2), α is the adsorption co-efficient, h and c are the Planck's constant and speed of light, ε_{real} and ε_{imag} are real and imaginary part of dielectric constant.

3.3 Results and Discussion

3.3.1 Structural and Electronic Properties of Pristine and Na, K and Ca Doped $SnSe_2$

Before evaluating the catalytic activities of $SnSe_2$ for HER and OER activities, a comprehensive analysis was conducted. This involved optimization of pristine and doped (Na, K, and Ca) $SnSe_2$ monolayer. The optimized geometries of pristine and doped monolayer are depicted in ***Figure 3.1(a)*** and ***Figure 3.1(b)*** respectively. The native state of the $SnSe_2$ monolayer adopts a 1T phase and space group P-3*m*1, similar to the SnS_2 structure, characterized by a Sn atom surrounded by Se atoms in an octahedral arrangement. The theoretical and experimental lattice parameter for the $SnSe_2$ unit cell was found to be around 3.823 Å [29,30]. In our calculations, a 2x2x1 supercell of the $SnSe_2$ monolayer was utilized, yielding optimized lattice constants and bond lengths of approximately 7.69 Å and 2.73 Å, respectively. This supercell size allowed for the accommodation of alkali metal dopants, in line with previous studies on similar materials [15,31-35].

To enhance the electrocatalytic performance of $SnSe_2$, S-block elements (Na, K, and Ca) were introduced into the monolayer, with a doping concentration of 25% achieved by replacing one Sn atom with the respective alkali metal. Notably, the addition of alkali metals did not significantly distort the $SnSe_2$ structure as observed in ***Figure 3.1***, as bond lengths such as Na-Se (2.73 Å), K-Se (3.06 Å), and Ca-Se (2.86 Å) remained close to the original $SnSe_2$ bond length. The electronic properties were influenced by dopants, impacting the electronegativity and subsequently modifying the work function.

Understanding the electronic properties is crucial in selecting suitable catalysts. Generally, metallic systems are preferred for effective electrocatalysis, while semiconducting systems with band gaps around 1-2 eV are favourable for photocatalysis or electro-photocatalysis. The electronic DOS was examined for both pristine and doped $SnSe_2$, revealing a band gap of 0.8 eV for $SnSe_2$ (see ***Figure 3.2***), which aligned with previous findings [19]. The introduction of different S group elements via Sn substitution lead to alterations in the electronic properties, resulting in a shift towards metallic behaviour. For a detailed assessment of H and O adsorption on these materials, simulations were conducted by adsorbing H and O atoms at the basal plane of the $SnSe_2$ monolayer and on the dopant sites as seen in ***Figure 3.3(a*** and ***b)***. The HER and OER activities were evaluated based on these adsorption configurations as shown in ***Table 3.1***. The data in ***Table 3.1*** provide valuable information for the potential catalytic applications of these systems.

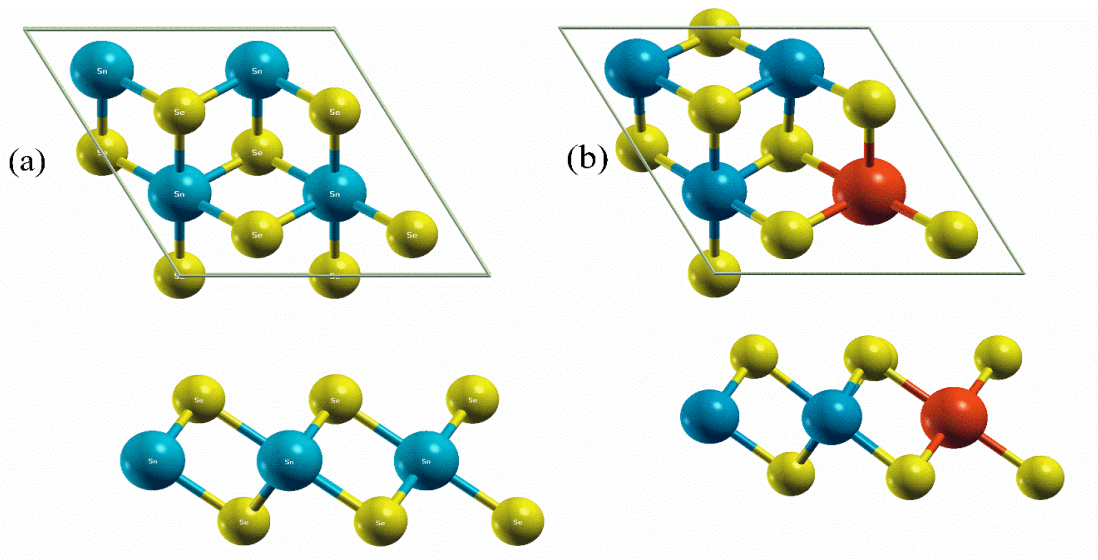

Figure 3.1: Top and side views of optimized geometries of (a) pristine $SnSe_2$ and (b) doped-$SnSe_2$. [4]

Table 3.1: Optimized lattice constant, bond length, work function, adsorption energy and Gibbs free energy of hydrogen and oxygen of $SnSe_2$ and doped-$SnSe_2$.

System	Lattice constant (Å)	Bond length (Å)	Work function ϕ(eV)	ΔE^H (eV)	ΔE^O (eV)	ΔG^H (eV)	ΔG^O (eV)
$SnSe_2$	7.659	2.73	5.95	0.55	-1.02	0.79	-0.69
Na-doped	7.501	2.73	5.91	-0.53	-0.87	-0.29	-0.54
K-doped	7.692	3.06	5.77	-1.53	-1.96	-1.29	-1.72
Ca-doped	7.597	2.86	6.10	0.48	-0.78	0.72	-0.45

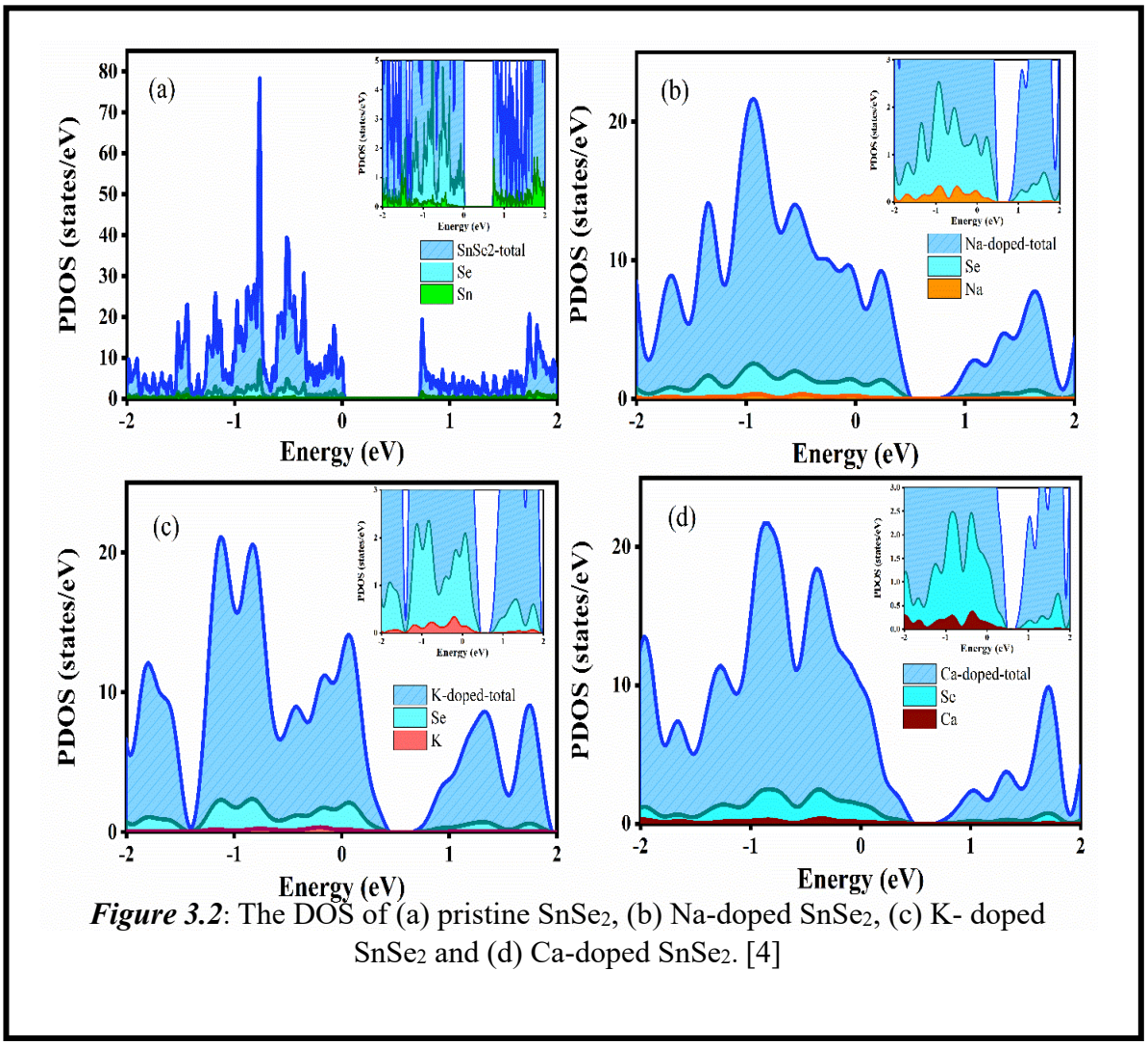

Figure 3.2: The DOS of (a) pristine $SnSe_2$, (b) Na-doped $SnSe_2$, (c) K- doped $SnSe_2$ and (d) Ca-doped $SnSe_2$. [4]

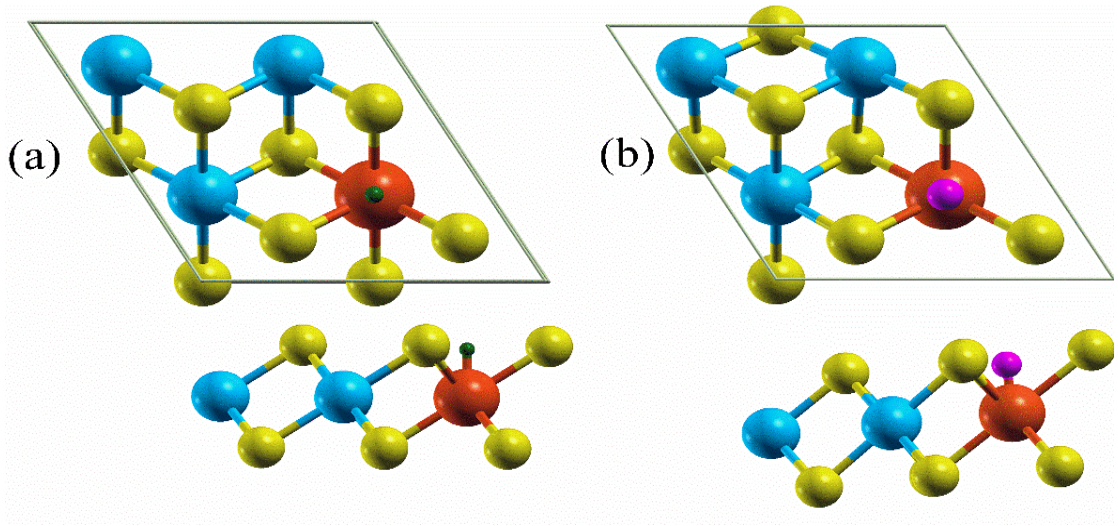

Figure 3.3: Top and side view of (a) hydrogen adsorbed and (b) oxygen adsorbed doped-$SnSe_2$. [4]

To gain insights into the impact of H and O adsorption on the electronic behaviour of both pristine and doped-$SnSe_2$, partial density of states (PDOS) calculations was performed and are depicted in ***Figure 3.4*** and ***3.5***. The PDOS graphs offer a visualization of changes in the electronic density of states resulting from the strong interactions between adsorbates and the host material. By observing the interaction of H and O near the fermi level, we can depict the level of adsorption of these atoms with the surface.

Analyzing the PDOS of H adsorption on the pristine $SnSe_2$ monolayer (shown in ***Figure 3.4(a)***), it's evident that H makes a more significant contribution to the conduction band (anti-bonding state) compared to the valence band region (bonding state) near the Fermi level. This suggests a relatively weak interaction with the Sn atom, indicating physisorption behaviour. In contrast, when considering alkali metal-doped $SnSe_2$ monolayers, the PDOS plots illustrate that H contribution near the Fermi level is less pronounced in the case of Na-doped $SnSe_2$ (shown in ***Figure 3.4(b)***). This implies that H tends to prefer adsorption on the edge site of Se atoms rather than on the basal plane. This preference is due to the oxidation state of Na

being +1, in contrast to Sn +2 oxidation state, leading to defect bonding in the Na-doped $SnSe_2$ monolayer. For the K-doped $SnSe_2$ (shown in ***Figure 3.4(c)***) monolayer, a notably

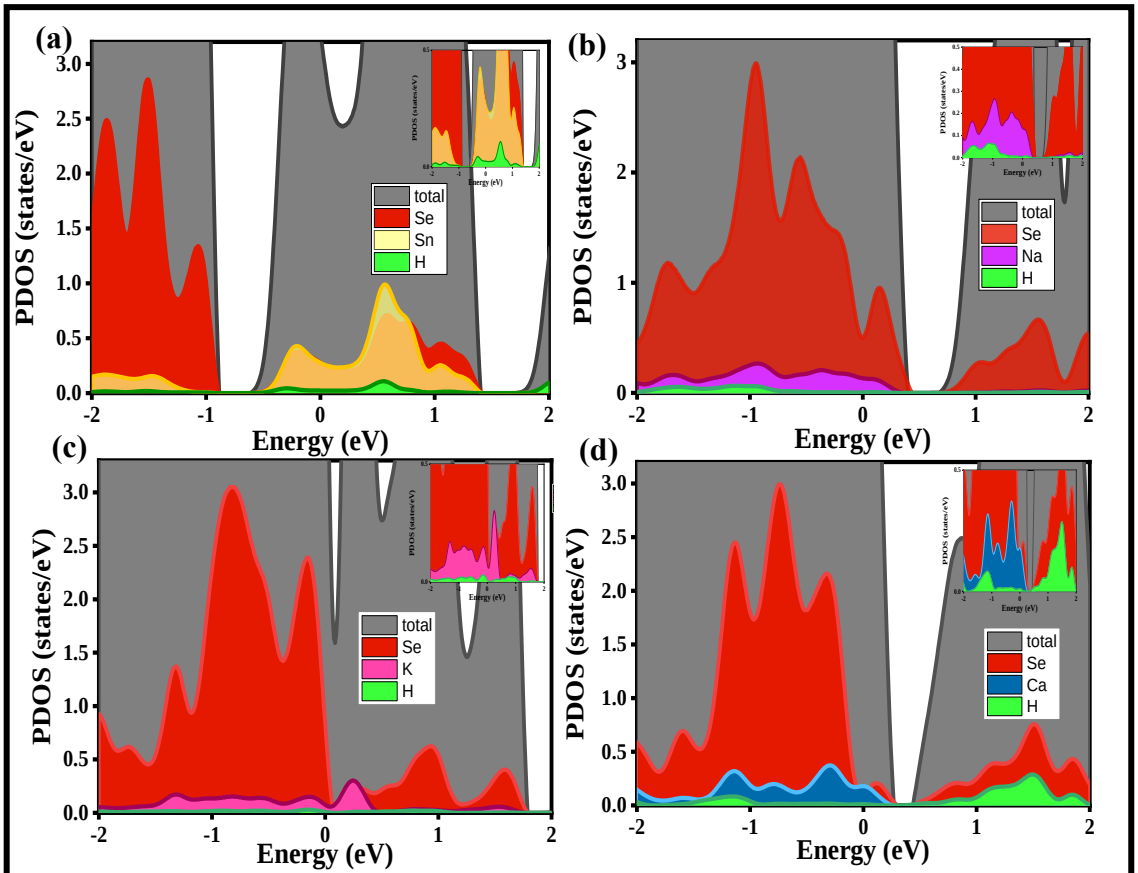

Figure 3.4: PDOS of hydrogen adsorbed on (a) $SnSe_2$ and doped ((b) Na, (c) K and (d) Ca)) $SnSe_2$ monolayer. [4]

higher contribution of the H atom toward the valence band region is observed, indicating chemisorption due to a strong interaction between H and the K-doped $SnSe_2$ monolayer. This interaction is stronger compared to other dopants. The significant contribution of the H atom to the valence band in both K and Na-doped $SnSe_2$ can be attributed to the formation of defect bonds arising from their +1oxidation state. Additionally, the preference of the H atom for Se edge-sites over the basal plane further amplifies its contribution to the valence band. In the context of Ca-doped $SnSe_2$ (shown in ***Figure 3.4(d)***), the contribution of the H atom to the conduction band resembles that of the pristine $SnSe_2$ monolayer, making it less favourable as

a catalyst for HER. In the scenario of O adsorption, chemisorption is observed in $SnSe_2$ (shown in ***Figure 3.5(a)***), differing from the behaviour during H adsorption. The higher contribution of O to the valence band than the conduction band results in a robust interaction between Sn and O. Notably, the contribution of O near the Fermi level is minimal in the case of Ca-doped $SnSe_2$ (shown in ***Figure 3.5(c)***), indicating that the Ca-doped $SnSe_2$ monolayer is more suitable as a catalyst for the OER when compared to the Na-doped $SnSe_2$ (shown in ***Figure 3.5(b)***). In summary, based on the insights gained from the PDOS calculations and charge transfer analysis, it can be concluded that Na-doped and Ca-doped $SnSe_2$ monolayers exhibit good catalytic activities for HER and OER, respectively (see ***Figure 3.4*** and ***3.5***). The distinct behaviours these materials in response to H and O adsorption are attributed to their electronegativities and interactions with the dopants. Additionally, we investigated the charge transfer that occurs during the adsorption of H and O atoms on both pristine and doped $SnSe_2$, utilizing Löwdin charge analysis. The results revealed that during H adsorption, electron accumulation occurs on the pristine and doped $SnSe_2$ surfaces, with values of approximately 0.53e, 0.05e, 0.07e, and 0.08e at Sn, Na, K, and Ca atoms, respectively. On the other hand, during O adsorption, electron depletion takes place at Sn, Na, K, and Ca atoms, with values of around 0.51e, 0.57e, 0.8e, and 0.6e, respectively. The outcomes of the charge transfer analysis indicate that during H adsorption, the lowest electron accumulation is observed in the case of Na-dopant, followed by K-dopant. Conversely, during O adsorption, the lowest electron depletion is evident for the pristine $SnSe_2$, followed by the Ca-dopant. These observations reflect the variations in electronegativity among the different elements. The trends in O and H interactions with the systems are distinct due to the higher electronegativity of O compared to H.

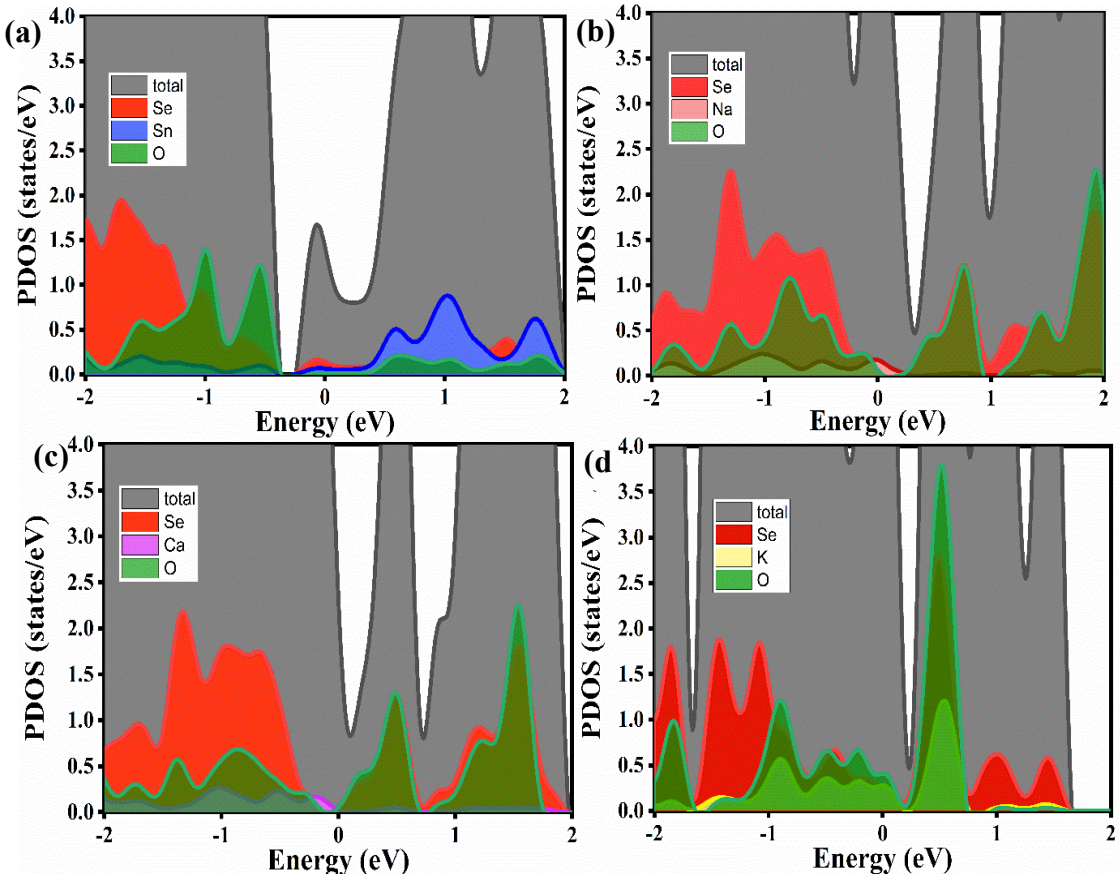

Figure 3.5: PDOS of oxygen adsorbed on (a) $SnSe_2$ and doped ((b) Na, (c) Ca and (d) K)) $SnSe_2$ monolayer. [4]

3.3.2 Optical Properties and Work-Function Analysis

To assess the potential of these systems as electro-photo catalysts, we conducted computations to determine the absorption spectra of both pristine and doped $SnSe_2$ monolayers. The optical absorption spectra provide crucial insights into fundamental characteristics such as the highest absorption range and absorption coefficients of the materials. Effective electro-photocatalytic activity requires that the energy surpasses the combined values of the band gap E_g and the energy necessary for photon absorption E_{AOP}, as outlined in equation (3.1). Analyzing the absorption spectra, as depicted in ***Figure 3.6***, we clearly observe that the $SnSe_2$ monolayer possesses an optical band gap of 1.2 eV. Moreover, the doped $SnSe_2$ monolayers

exhibit distinct absorption peaks within the range of 4 to 6.5 eV, indicating a demand for high-energy photons to trigger excitation in the system. Consequently, all the investigated $SnSe_2$ systems exhibit the potential to function as high-energy photo-electro catalysts.

Furthermore, we conducted computations to determine the work function (φ) of these systems, providing support for the results obtained from our analysis of HER and OER. The φ signifies the minimum energy necessary to remove an electron from a material's surface. In cases involving metals, the φ and ionization energy are equivalent. The φ is significantly influenced by surface conditions; even minor contamination within a monolayer can lead to adjustments in surface reactions, thereby altering the φ magnitude. The work function (φ) is defined as the energy difference between the vacuum level or electrostatic potential (V_1) and the Fermi energy (E_F) of the system.

$$\Phi = V_1 - E_F \tag{3.3}$$

The computed φ values for pristine and doped $SnSe_2$ monolayers are illustrated in ***Figure 3.7.*** The graphs exhibit notable differences in terms of the E_F value and the V_1. The impact of the change in bond length in K-doped $SnSe_2$ is evident as its behaviour deviates asymmetrically compared to the other cases. An observable trend is that the φ magnitude decreases with the incorporation of Na and K dopants. Conversely, doping with a Ca atom leads to an increase in the φ from 5.95 eV to 6.10 eV (as indicated in ***Table 3.1***). This increase can be attributed to the electronegativity phenomenon. The electronegativity values for Na, K, and Ca-doped systems are 0.93, 0.82, and 1.00, respectively. Higher electronegativity values indicate stronger element binding, requiring more energy to excite electrons to the conduction band. Consequently, the φ increases in comparison to the other dopants. It's noteworthy that the φ magnitudes of the pristine, Na-doped, and K-doped $SnSe_2$ monolayers fall within the ranges of effective HER catalysts such as Pt and Pd, which possess φ values of approximately 5.12 and 5.7 eV,

respectively [36]. This observation further corroborates the promising catalytic activity of Na- and Ca-doped $SnSe_2$ monolayers for HER and OER, respectively.

In the context of water electrolysis devices, which involve a cathode for the HER and an anode for OER, a certain electrostatic potential is applied to these electrodes to initiate the water-splitting process [37]. The catalyst thermodynamic voltage typically exceeds 1.23 V at 25°C and 1 atm, serving as an overpotential required to initiate water splitting. The relationship between the free energy of the hydrogen adsorbed state and the exchange current density of HER, expressed through the Sabatier relationship [38,39], offers insights into the HER and OER performances of the systems under consideration. The efficiency of HER and OER catalysis is determined by the exchange current density, directly related to Gibbs free energy (ΔG^H), within an equilibrium condition as defined in the provided expression,

$$\Delta G^X = \Delta E^X_{ads} + \Delta E^X_{ZPE} - T\Delta S^X \quad (3.4)$$

Here, the symbol *X* represents either a H or O atom. $\boldsymbol{E^X_{ads}}$ denotes the adsorption energy of the system with *X* atom adsorbed, and $\Delta\boldsymbol{E^X_{ZPE}}$ represents the zero-point energy difference between *X* atoms in the adsorbed and gas phases. Additionally, *T* signifies temperature, and ΔSX accounts for the entropy of *X*. The corresponding ΔG^x for the H and O adsorbed systems can be expressed as: $\Delta G^H = E^H_{ads} + 0.24$ and $\Delta G^O = E^O_{ads} + 0.33$ respectively; as the terms $\Delta\boldsymbol{E^X_{ZPE}}$ and $\mathbf{T\Delta S^X}$ get reduced to 0.24 and 0.33 for H and O adsorption respectively. The chemisorption energies of H and O adsorption are defined as:

$$E^X_{ads} = E_{(system + X)} - E_{(system)} - \frac{1}{2}E_{(X2)} \quad (3.5)$$

In essence, these equations provide a framework for calculating the ΔG^x and chemisorption energies, allowing us to assess the thermodynamic aspects of H and O adsorption on the material surfaces. Where, $E_{(system+X)}$ is total energies of $SnSe_2$ or doped-$SnSe_2$ monolayer

subjected to H or O adsorption, $E_{(system)}$ is total energy of $SnSe_2$ or doped-$SnSe_2$ monolayer and $E_{(X2)}$ stands for total energy of isolated H_2 or O_2 molecule. For a highly efficient HER catalyst, the magnitude of ΔG^H should be close to zero. A high positive value of ΔG^H implies weaker H adsorption, making the Volmer step of water-splitting challenging. Conversely, a highly negative value of ΔG^H indicates strong H adsorption on the adsorbate, which can hinder the overall hydrogen evolution process. The highly negative value for the ΔE^H and ΔG^H magnitudes indicates a strong binding of H atom to the K-doped $SnSe_2$ monolayer. This strong binding presents a challenge for the Heyrovsky or Tafel step, involving the desorption of hydrogen molecules [40]. Analyzing the magnitudes of ΔE^H and ΔG^H (refer to ***Table 3.1***), it can be concluded that H exhibits robust bonding with the K-doped $SnSe_2$ monolayer due to the overly negative value, signifying a hindered desorption process. Conversely, for the pristine and Ca-doped $SnSe_2$ monolayers, the positive values of both ΔE^H and ΔG^H imply weaker H adsorption. Among all the systems considered, the ΔG^H of Na-doped $SnSe_2$ possesses the lowest value, nearly approaching zero, particularly for H adsorption. This observation indicates that the Na-doped $SnSe_2$ monolayer is exceptionally well-suited for catalysis of HER activity. In the context of O adsorption, the Ca-doped $SnSe_2$ monolayer exhibits commendable catalytic activity for OER, followed by the Na-doped and pristine $SnSe_2$ monolayers.

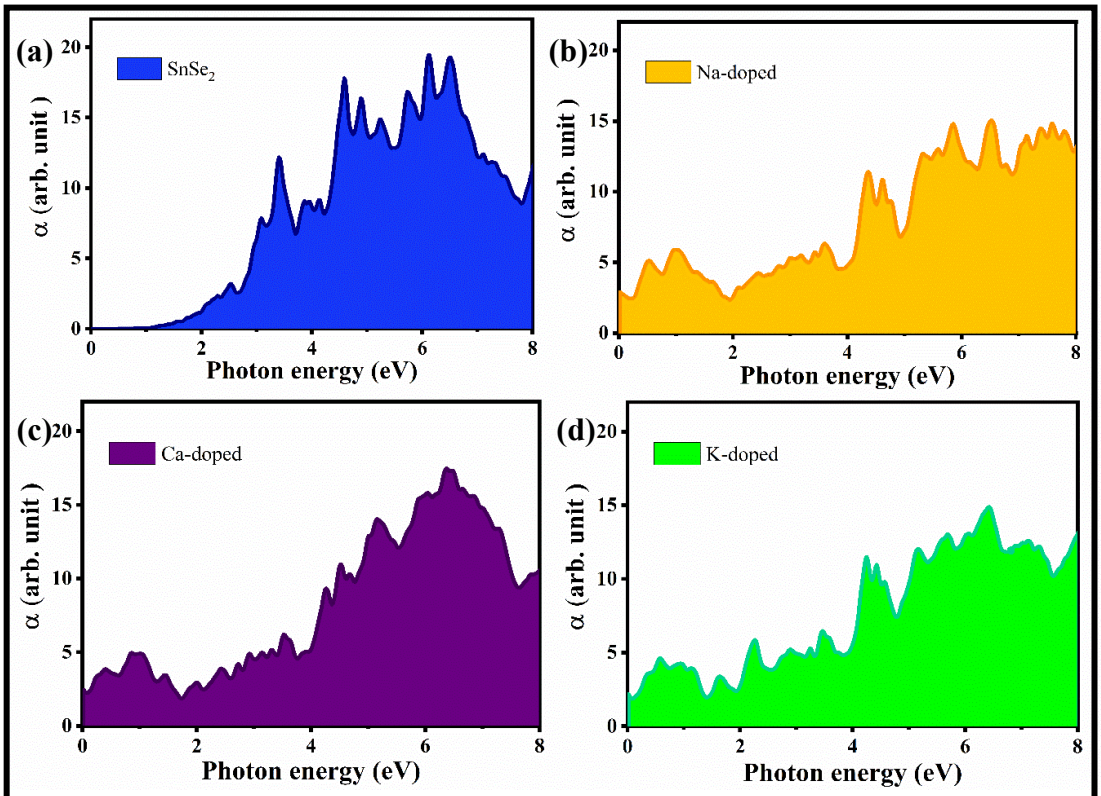

Figure 3.6: Plot for photon energy (a) pristine $SnSe_2$, (b) Na, (c) Ca and (d) K-doped $SnSe_2$ monolayers. [4]

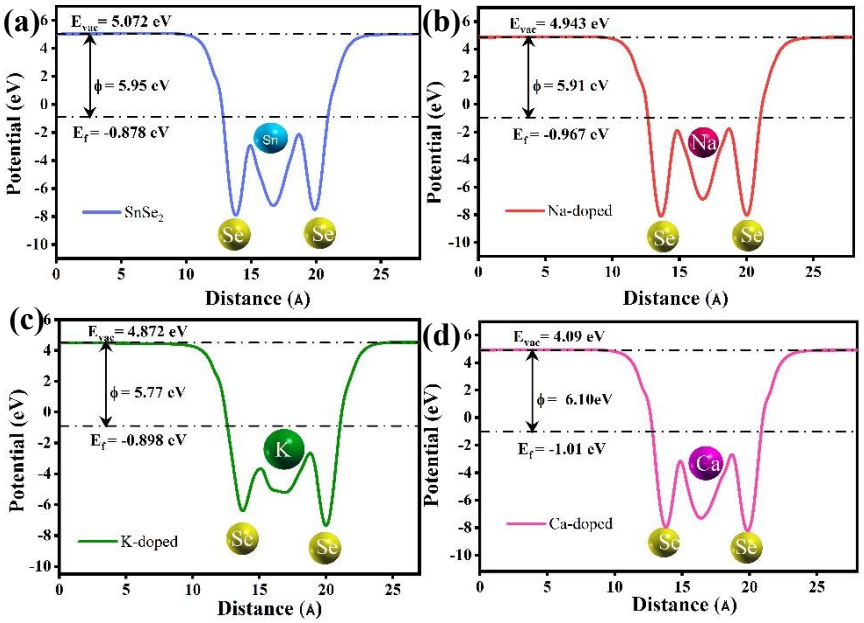

Figure 3.7: Work function of (a) pristine $SnSe_2$ and ((b) Na, (c) K and (d) Ca) doped-$SnSe_2$ monolayers. [4]

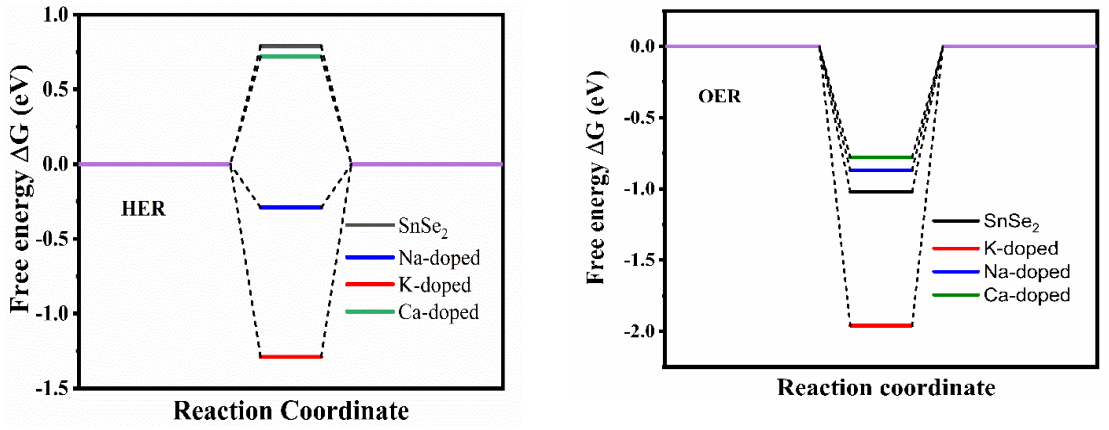

Figure 3.8: Reaction coordinate (a) HER and (b) OER of pristine $SnSe_2$ and doped-$SnSe_2$.

3.4 Conclusions

In summary, our study involved systematic investigations of the structural and electronic properties of pristine and alkali metal-doped $SnSe_2$ monolayers, utilizing first-principles based density functional theory. Our DOS analysis revealed that the pristine $SnSe_2$ monolayer exhibited a semiconductor nature, while the introduction of alkali metal dopants resulted in a transformation to a metallic state. We conducted a comprehensive analysis of H adsorption, focusing on site-dependent differences in adsorption capabilities across the $SnSe_2$ monolayers. Our findings demonstrated that for both the pristine and Na-doped $SnSe_2$ monolayers, the edge-site exhibited the highest favourability for H adsorption. In contrast, the basal plane demonstrated significant activity for Ca and K-doped $SnSe_2$ monolayers. Regarding O adsorption, the basal plane emerged as the most favourable site for both pristine and doped $SnSe_2$ monolayers. Through assessment of ΔG^x, we identified the potential of these materials to serve as catalysts for HER or OER. Specifically, the Na-doped $SnSe_2$ monolayer showcased suitability for HER catalysis due to its proximity to a zero ΔG^H. For OER catalysis, the Ca-doped $SnSe_2$ monolayer exhibited promise, followed by Na-doped and pristine $SnSe_2$

monolayers. To encapsulate, our study signifies that the catalytic activity of the $SnSe_2$ monolayer can be significantly enhanced through the incorporation of alkali metals dopant.

References

1. J. A. Turner, *Science (1979)*, 1999, **285**, 687–689.
2. M. MOMIRLAN and T. VEZIROGLU, *Int J Hydrogen Energy*, 2005, **30**, 795–802.
3. T. Bak, J. Nowotny, M. Rekas and C. C. Sorrell, *Int J Hydrogen Energy*, 2002, **27**, 991–1022.
4. A. N. Inamdar, N. N. Som, A. Pratap and P. K. Jha, *Int J Hydrogen Energy*, 2020, **45**, 18657–18665.
5. A. Eftekhari and B. Fang, *Int J Hydrogen Energy*, 2017, **42**, 25143–25165.
6. R. Li and C. Li, *Advances in Catalysis*, 2017, **60**, 1–57.
7. J. Di, C. Yan, A. D. Handoko, Z. W. Seh, H. Li and Z. Liu, *Materials Today*, 2018, **21**, 749–770.
8. L. Mascaretti, S. Ferrulli, P. Mazzolini, C. S. Casari, V. Russo, R. Matarrese, I. Nova, G. Terraneo, N. Liu, P. Schmuki and A. Li Bassi, *Solar Energy Materials and Solar Cells*, 2017, **169**, 19–27.
9. D. P. Kumar, V. D. Kumari, M. Karthik, M. Sathish and M. V. Shankar, *Solar Energy Materials and Solar Cells*, 2017, **163**, 113–119.
10. M. Alizadeh, G. B. Tong, M. S. Mehmood, K. W. Qader, S. A. Rahman and B. Shokri, *Solar Energy Materials and Solar Cells*, 2018, **185**, 445–455.
11. B. R. Sathe, X. Zou and T. Asefa, *Catal. Sci. Technol.*, 2014, **4**, 2023–2030.
12. A. V. Dolganov, O. V. Tarasova, A. Y. Ivleva, O. Y. Chernyaeva, K. A. Grigoryan and V. S. Ganz, *Int J Hydrogen Energy*, 2017, **42**, 27084–27093.
13. S. H. Mir, S. Chakraborty, P. C. Jha, J. Wärnå, H. Soni, P. K. Jha and R. Ahuja, *Appl Phys Lett*,2016, **109(5)**.
14. S. H. Mir, S. Chakraborty, J. Wärnå, S. Narayan, P. C. Jha, P. K. Jha and R. Ahuja, *Catal Sci Technol*, 2017, **7**, 687–692.
15. N. N. Som, V. Mankad and P. K. Jha, *Int J Hydrogen Energy*, 2018, **43**, 21634–21641.
16. S. B. Pillai, S. D. Dabhi and P. K. Jha, *Int J Hydrogen Energy*, 2018, **43**, 21649–21654.
17. J. KUBISZTAL, A. BUDNIOK and A. LASIA, *Int J Hydrogen Energy*, 2007, **32**, 1211–1218.
18. M.-R. Gao, M. K. Y. Chan and Y. Sun, *Nat Commun*, 2015, **6**, 7493.

19. X. Wu, J. Han, Y. Feng, G. Li, C. Wang, G. Ding and G. Gao, *RSC Adv*, 2017, **7**, 44499–44504.C.
20. Sun, J. Zhang, J. Ma, P. Liu, D. Gao, K. Tao and D. Xue, *J Mater Chem A Mater*, 2016, **4**, 11234–11238.
21. G. Long, K. Wan, M. Liu, Z. Liang, J. Piao and P. Tsiakaras, *J Catal*, 2017, **348**, 151–159.
22. S. Dong and Z. Wang, *Beilstein Journal of Nanotechnology*, 2018, **9**, 1820–1827.
23. L. Wang, X. Chen, H. Du, Y. Yuan, H. Qu and M. Zou, *Appl Surf Sci*, 2018, **427**, 1030–1037.
24. P. Reunchan and S.-H. Jhi, *Appl Phys Lett*, 2011, **98 (9)**.
25. Y. Li, X. Ding and Q. Zhang, *Sci Rep*, 2016, **6**, 31144.
26. P. Giannozzi, S. Baroni, N. Bonini, M. Calandra, R. Car, C. Cavazzoni, D. Ceresoli, G. L. Chiarotti, M. Cococcioni, I. Dabo, A. Dal Corso, S. de Gironcoli, S. Fabris, G. Fratesi, R. Gebauer, U. Gerstmann, C. Gougoussis, A. Kokalj, M. Lazzeri, L. Martin-Samos, N. Marzari, F. Mauri, R. Mazzarello, S. Paolini, A. Pasquarello, L. Paulatto, C. Sbraccia, S. Scandolo, G. Sclauzero, A. P. Seitsonen, A. Smogunov, P. Umari and R. M. Wentzcovitch, *Journal of Physics: Condensed Matter*, 2009, **21**, 395502.
27. J. P. Perdew, K. Burke and Y. Wang, *Phys Rev B*, 1996, **54**, 16533–16539.
28. H. J. Monkhorst and J. D. Pack, *Phys Rev B*, 1976, **13**, 5188–5192.
29. J. M. Gonzalez and I. I. Oleynik, *Phys Rev B*, 2016, **94**, 125443.
30. M. Schlüter and M. L. Cohen, *Phys Rev B*, 1976, **14**, 424–431.
31. S. Ma, D. Yuan, Z. Jiao, T. Wang and X. Dai, *The Journal of Physical Chemistry C*, 2017, **121**, 24077–24084.
32. X. Yu, Y. Li, J. Cheng, Z. Liu, Q. Li, W. Li, X. Yang and B. Xiao, *ACS Appl Mater Interfaces*, 2015, **7**, 13707–13713.
33. M. A. Othman, B. H. Ahmad and N. F. Amat, *JSTS:Journal of Semiconductor Technology and Science*, 2013, **13**, 635–646.
34. D. Upadhyay, B. Roondhe, A. Pratap and P. K. Jha, *Appl Surf Sci*, 2019, **476**, 198–204.
35. S. S. Chou, N. Sai, P. Lu, E. N. Coker, S. Liu, K. Artyushkova, T. S. Luk, B. Kaehr and C. J. Brinker, *Nat Commun*, 2015, **6**, 8311.
36. H. B. Michaelson, *J Appl Phys*, 1977, **48**, 4729–4733.
37. S. Wang, A. Lu and C.-J. Zhong, *Nano Converg*, 2021, **8**, 4.
38. J. K. Nørskov, T. Bligaard, A. Logadottir, J. R. Kitchin, J. G. Chen, S. Pandelov and U. Stimming, *J Electrochem Soc*, 2005, **152**, J23.

39. J. Greeley, T. F. Jaramillo, J. Bonde, I. Chorkendorff and J. K. Nørskov, *Nat Mater*, 2006, **5**, 909–913.

40. Q. Ding, B. Song, P. Xu and S. Jin, *Chem*, 2016, **1**, 699–726.